Nanopatterning dynamics on Si(100) during oblique 40-keV Ar^+ erosion with metal codeposition: Morphological and compositional correlation

A. Redondo-Cubero,[1,2] R. Gago,[1] F. J. Palomares,[1] A. Mücklich,[3] M. Vinnichenko,[3] and L. Vázquez[1,*]

[1]*Instituto de Ciencia de Materiales de Madrid, Consejo Superior de Investigaciones Científicas, 28049 Madrid, Spain*

[2]*Instituto Tecnológico e Nuclear, Instituto Superior Técnico, Universidade Técnica de Lisboa, 2686-953 Sacavém, Portugal*

[3]*Institute of Ion Beam Physics and Materials Research, Helmholtz-Zentrum Dresden-Rossendorf, D-01314 Dresden, Germany*

(Received 2 April 2012; revised manuscript received 22 June 2012; published 20 August 2012)

The formation and dynamics of nanopatterns produced on Si(100) surfaces by 40-keV Ar^+ oblique ($\alpha = 60^\circ$) bombardment with concurrent Fe codeposition have been studied. Morphological and chemical analysis has been performed by *ex situ* atomic force microscopy, Rutherford backscattering spectrometry, x-ray photoelectron spectroscopy, and scanning and transmission electron microscopies. During irradiation, Fe atoms incorporated into the target surface react with Si to form silicides, a process enhanced at this medium-ion energy range. The silicides segregate at the nanoscale from the early irradiation stages. As the irradiation proceeds, a ripple pattern is formed without any correlation with silicide segregation. From the comparison with the pattern dynamics reported previously for metal-free conditions, it is demonstrated that the metal incorporation alters both the pattern dynamics and the morphology. Although the pattern formation and dynamics are delayed for decreasing metal content, once ripples emerge, the same qualitative pattern of morphological evolution is observed for different metal content, resulting in an asymptotic saw-tooth-like facetted surface pattern. Despite the medium ion energy employed, the nanopatterning process with concurrent Fe deposition can be explained by those mechanisms proposed for low-ion energy irradiations such as shadowing, height fluctuations, silicide formation and segregation, ensuing composition dependent sputter rate, and ion sculpting effects. In particular, the interplay between the ion irradiation and metal flux geometries, differences in sputtering rates, and the surface pattern morphology produces a dynamic compositional patterning correlated with the evolving morphological one.

DOI: 10.1103/PhysRevB.86.085436 PACS number(s): 81.16.Rf, 68.35.Ct, 79.20.Rf

I. INTRODUCTION

Ion beam sputtering (IBS) has become an interesting and powerful technique for surface nanopatterning. Among its advantages, we can highlight its versatility, efficiency, and capability to induce (mostly dotted or rippled) nanopatterns in a wide range of targets including semiconductors, metals, and insulators over relatively wide surface areas (up to several tens of cm^2) in short times (typically a few minutes).[1,2] Furthermore, IBS nanopatterns are being employed as templates for the growth of magnetic[3] or plasmonic[4] nanostructures, and also for other technological applications.[5–7]

During the last few years, the key role played by the unintended simultaneous supply of impurities and metal atoms in IBS pattern formation has become manifest, especially in the case of monoelemental targets.[8–11] Following this experimental evidence, detailed IBS experiments have been performed under impurity-free conditions on pure Si surfaces. Such studies revealed that IBS produces surface nanopatterns on Si only above a certain threshold (in the 45°–50° range) of the ion incidence angle α, with respect to the surface normal.[12–14] Likewise, several mechanisms have been proposed theoretically to account for this angle threshold, based either on mass redistribution[12,13,15–17] or on ion-induced solid flow.[14,18,19] Under this new experimental and theoretical scenario, the previous reports on IBS pattern formation below this threshold angle (especially those reporting nanodot pattern formation under normal incidence) should be interpreted as being due to the (inadvertent) presence of impurities during IBS.[11,20] Despite the complexity added by the (usually undesirable) presence of metal impurities, IBS pattern formation with concurrent metal deposition is emerging as both a strategy to tune the pattern properties and a framework to better understand IBS nanopatterning of multicomponent systems.[21–24] This interest has led to the development of specific theoretical models on IBS nanopatterning with concurrent metal deposition.[25–27] On the other hand, it has motivated recent, rather systematic, experimental works (mainly, focused on silicon)[28–30] aimed at understanding the mechanisms behind the pattern formation under these conditions. It should be noted that these works have addressed only the case of low-energy (1–5 keV) IBS.

The present work, which is inscribed within this experimental framework, is focused on understanding how the simultaneous metal incorporation affects the IBS pattern formation and dynamics. As a novelty, we study the unexplored ion medium-energy range by working at an ion energy (40 keV) roughly one order of magnitude higher than those studied in the aforementioned works. These conditions imply a larger ion penetration length, ion-induced amorphization, and sputtering rates that could lead to different pattern formation and dynamics. As recent reports have proposed different mechanisms for the pattern formation, the second goal of our work consists of determining whether they are also operative at this higher ion energy range. In contrast to the effort already focused on studying how the metal incorporation influences the pattern formation, the analysis of its impact on the pattern dynamics is still scarcely addressed. Consequently, the third objective of this work refers to the investigation of this issue.

In order to assess the role of the concurrent metal deposition in the pattern dynamics, we have compared our results with

those reported by Chini *et al.*[31–34] under metal-free irradiation conditions for irradiation angles above the threshold angle ($\alpha = 60^\circ > 45^\circ$). Finally, the IBS experiments with concurrent Fe deposition were carried out following the experimental setup used in Refs. 28–30. This kind of study requires a rather systematic morphological and compositional characterization. Therefore, the morphology of the surface patterns produced in this work has been studied by atomic force microscopy (AFM), conductive-mode AFM (C-AFM) and, occasionally, by scanning (SEM) and transmission (TEM) electron microscopies. In parallel, compositional analysis has been performed by x-ray photoelectron spectroscopy (XPS), Rutherford backscattering spectrometry (RBS), and energy dispersive x-ray spectroscopy (EDX). With this set of techniques, we have been able to address the study of the correlation between the Fe content and the IBS induced pattern morphology and dynamics and to pursue the objectives mentioned above.

II. EXPERIMENT

The irradiation experiments were performed with a 40-keV Ar^+ beam extracted from a Danfysik 1090 ion implanter with a base pressure of 5×10^{-6} mbar. The ions impinged on the single-crystal Si(100) targets (1×1 cm^2) at $\alpha = 60^\circ \pm 5^\circ$ with respect to the surface normal with a current density of 18 μA cm^{-2} in the sample plane. A steel plate (1.5 mm high) placed adjacent to the Si target acted simultaneously as an Fe source and a sample holder. To obtain homogeneous irradiation, the focused beam was scanned with a magnetic x-y sweeping system in such way that both the Si surface and the steel target were bombarded. The irradiation times spanned from 20 min to 16 h, implying doses up to $\sim 6.5 \times 10^{18}$ ions/cm^2.

The resulting surface morphology was imaged *ex situ* by AFM operating in the dynamic mode with Nanoscope IIIa equipment (Veeco©) and with an Agilent PicoPlus 5500, the latter being able to operate in C-AFM.[35–37] Silicon cantilevers, with a nominal radius r of 8 nm and opening angle θ smaller than 52°, were employed for the topographical measurements, whereas either Pt coated (OMCL-AC240TM, $r < 25$ nm and $\theta < 70^\circ$, from Olympus and DPER18, $r \sim 15$ nm and $\theta < 32^\circ$, from MikroMasch) or diamond coated (CDT-FMR, $r \sim 83 \pm 17$ nm and $\theta < 47^\circ$, from NanoWorld, and DCP11, $r \sim 60 \pm 10$ nm and $\theta < 44^\circ$, from NT-MDT) tips were employed for the AFM electrical modes. In the C-AFM mode, imaging biases in the 3–9 V range at both polarities were employed. These measurements were performed under a nitrogen atmosphere to avoid contributions from the water vapor adsorbed on the surface.

The surface roughness σ was obtained from the AFM images using the equipment software. Other image analyses were made with the Gwyddion freeware package.[38] In addition, the characteristic wavelength of the ripple pattern λ was obtained from the power spectral density (PSD) of the images as follows. The PSD is defined as $\mathrm{PSD}(k,t) = \langle H(k,t)H(-k,t)\rangle$, where $H(k,t)$ is the Fourier transform of the surface height of the one-dimensional cut $h(r,t) - \langle h\rangle$, where $\langle h\rangle$ stands for the average height of this profile, and k is the spatial frequency. We have obtained the corresponding PSD curves along both the parallel ($\mathrm{PSD}_\parallel$) and perpendicular ($\mathrm{PSD}_\perp$) directions to the projected direction of the ion beam. Since ripple patterns are produced with the wave vector parallel to the projected ion beam, the spatial frequency k_0 of the peak in the $\mathrm{PSD}_\parallel$ gives the value of λ since $k_0 = 1/\lambda$. When a facetted pattern is formed, the corresponding $\mathrm{PSD}_\parallel$ displays, in a logarithmic plot, a linear region for high k values and a sort of saturated behavior for low k values. In this case, k_0 is taken at the crossover between both regions.

The SEM measurements were performed with NOVA NANOSEM 230 equipment (FEI) operating with a low-voltage–high-contrast detector. This equipment allowed EDX analysis over selected areas of the sample surface. Cross-sectional specimens for high-resolution TEM (HR-TEM) measurements were prepared by gluing two slices of the sample onto Ti disks, followed by mechanical polishing and conventional Ar^+ ion thinning (furnished with 3 keV ion energy) to electron transparency. The samples were examined with an image-corrected TITAN 80-300 (FEI) microscope operated at 300 kV and equipped with a retractable EDX detector.

The composition of the nanopatterned surfaces was determined by means of RBS. A 2 MeV He^+ beam (1 mm^2 size) was used, and the backscattered particles were detected with a Si solid-state detector at a scattering angle of 170°. RBS spectra in channeling (RBS/C) and random geometries were acquired to characterize the ion-induced amorphous layer (a-layer) on the target surface. In addition, high-resolution XPS data were acquired with a SPECS Phoibos 150 spectrometer with a hemispherical analyzer using monochromatic Al K_α radiation. Fe $2p$ and Si $2p$ core-level XPS spectra were recorded using an energy step of 0.05 eV and a pass energy of 10 eV, which provides an overall energy resolution of ~0.40 eV. The spectra were acquired at take-off angles from normal (90°) to grazing (15°) emission in order to study correlations between surface morphology and the composition. Note that, under grazing emission, the signal from the outermost surface region is also enhanced. Data analysis was performed using the Casa XPS processing software (Casa Software Ltd., Cheshire, UK). The integral peak areas after background subtraction and normalization using sensitivity factors were used to calculate the atomic concentration of each element.

Finally, sputter yield calculations for Si and Fe-Si compounds and angular distribution for the sputtered Fe atoms and the scattered primary Ar^+ ions were performed with TRIM code.[39]

III. RESULTS

A. Compositional and chemical analysis of the irradiated targets: RBS and XPS

The experimental setup, in which a steel target is located at one extreme of the silicon surface, allows the concurrent deposition of sputtered Fe atoms during irradiation of the Si surface. Obviously, as reported by Macko *et al.*,[28,30] the farther the landing spot from the steel target, the lower the expected deposition (flux) of Fe. Once the Fe atoms are deposited onto the Si surface they will be (again) prone to be resputtered by the direct Ar^+ ion beam. Therefore, we have to determine the metal content

as a function of the distance (in the millimeter range) to the metal target and the irradiation time for the different samples.

First, we have performed RBS/C measurements at different distances d from the metal source for a given time and for different times at a fixed location.[40] It was clearly observed that the Fe yield (content) increases for lower d (as expected) and with implantation time (dose). This Fe content corresponds to average compositions ranging between 3% (for large d and/or early times) and 20% (for low d and/or long times). Also, the broadness and low energy of the Fe yield tail[40] indicate that Fe atoms are not constrained within the near-surface regions, but have an in-depth profile within the a-layer. Obviously, the trend in the Si content is the opposite of that mentioned for Fe.

The RBS analysis of the Fe content evolution with Ar^+ fluence was studied in detail at two locations on the Si surface, namely, $d = 3$ and 5 mm away from the steel target. The analysis was done by integrating the Fe yield and calculating the corresponding areal density from the scattering cross section and measurement conditions. Figure 1(a) shows the change of the Fe content with irradiation time at those distances. At $d = 3$ mm, the Fe content initially increases monotonically and reaches a steady-state Fe surface coverage of $\sim 10^{17}$ at/cm^2 after 4 h of irradiation. This value is roughly one order of magnitude higher than the steady-state coverage observed in similar setups but operating with low-energy ion beams.[29,30] This difference can be explained by the appreciably higher ion energies employed in our system that induce in-depth ion beam mixing and radiation enhanced diffusion,[41] resulting in Fe incorporation into larger depths. For $d = 5$ mm, the Fe content increases with irradiation time up to $\sim 3 \times 10^{16}$ at/cm^2, although saturation can only be guessed after 12 h of irradiation. Note that, for any irradiation time, the content measured at $d = 5$ mm is always lower than the corresponding content obtained at 3 mm. In addition, the error bars for the values at $d = 5$ mm are larger since the lateral homogeneity of the Fe content at this location is poorer (probably due to the low content and broad distribution of the incoming Fe atoms).

In order to obtain further insight into the incorporation of Fe atoms on the Si irradiated surface, we performed XPS analysis of the sample irradiated for 8 h. Figure 1(b) displays the Fe atom distribution as a function of the distance to the steel target. Clearly there is a maximum located around 1.5 mm away from the steel target. Farther from this spot, the Fe content diminishes monotonously. This behavior is akin to that observed by Macko *et al.*[30] for low-energy Xe^+ irradiations. In fact, the measured residual Fe profile is a consequence of the specific Si target and steel clamp arrangement. Thus, whereas the primary Ar^+ ion beam impinges on the silicon surface with an angle of 60° with respect to the surface normal, it hits the (vertical) steel surface at an angle of 30° with respect to its surface normal. From the interaction of the incoming ion beam with the steel target, both sputtered Fe atoms and scattered primary Ar^+ ions are ejected from the surface but with different angular distributions [see the scheme in the top panel of Fig. 1(b)]. In analogy with the work by Macko *et al.*,[28] we have performed TRIM calculations of both angular distributions employed in our system. The sputtered Fe atoms leave the surface with a relatively broad angular distribution of $\sim \cos^n \theta$ (with n close to 2)[42] and hence, the most probable emission angle occurs along the normal to the steel surface. This leads to an important Fe flux on the Si surface, which decreases with d, and impinges on the Si surface with a very glancing angle (of just a few degrees at the farther locations). In contrast, the scattered primary Ar^+ ions leave the steel vertical wall with a substantial energy and a narrower angular distribution with the most probable angle around the specular direction.[39] Thus, those regions in the Si surface located alongside the steel target are simultaneously hit by both the primary Ar^+ ions and those scattered from the steel target which results in enhanced erosion. This enhanced erosion would produce the observed relative decrease of Fe atoms close to the steel target.

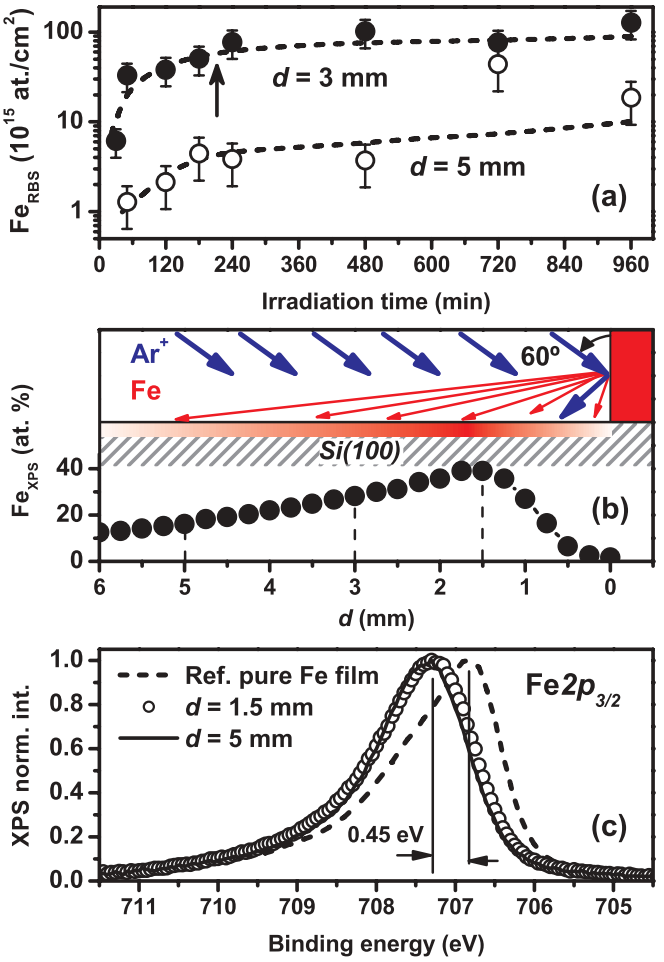

FIG. 1. (Color online) (a) Fe content change with irradiation time, extracted from RBS data at $d = 3$ and 5 mm. The arrow indicates the shadowing threshold time for the $d = 3$ mm location (see discussion). (b) Fe content profile as a function of the distance from the Fe target obtained from XPS measurements in the sample irradiated during 480 min. The top part depicts the sample setup and Ar^+/Fe fluxes to interpret the measured profile. Finally, the vertical dashed lines in the profile indicate the distances selected for a detailed AFM analysis. (c) Typical high-resolution XPS spectra obtained at normal emission on two different spots (1.5 and 5 mm) of the 8 h irradiated sample together with the spectrum of a reference Fe film grown by laser ablation. The chemical shift with respect to the Fe film observed for the irradiated samples is indicated.

The high-resolution XPS spectra of the Fe $2p_{3/2}$ core-level obtained at normal emission on two different spots (i.e., distances from the steel target) are displayed in Fig. 1(c). This figure also displays the spectrum measured using the same experimental conditions on a pure Fe film grown by laser ablation as a reference for Fe $2p$ core level of Fe-Fe bonds. The latter was measured after cleaning the film surface by ion bombardment to remove surface contamination and the outermost layers of oxidized Fe. The spectra measured for the 8 h irradiated sample readily show a clear chemical shift to a higher binding energy of ∼0.45 eV for the Fe $2p_{3/2}$ core level (irrespective of the surface location) which is similar to the 0.4 eV value reported for $FeSi_2$.[43] Accordingly, this silicide composition can be taken as the average one at the near surface region (slightly higher than the results determined by RBS where larger depths are sampled). A similar Fe $2p_{3/2}$ shift has been obtained in samples irradiated at lower fluences (not shown). Note also, that an appreciable formation of iron oxide can be ruled out because of the reduced intensity of Fe $2p_{3/2}$ at the position of Fe-O sites around 709.4 eV.[44] Therefore, we can state that almost all the incorporated Fe atoms tend to form silicide under our irradiation conditions. Another interesting feature of the spectra in Fig. 1(c) refers to the asymmetry in the Fe $2p_{3/2}$ core level. The line shape of the Fe film spectrum is rather asymmetric due to its metallic character.[44,45] In contrast, the spectra of IBS samples are rather symmetric.

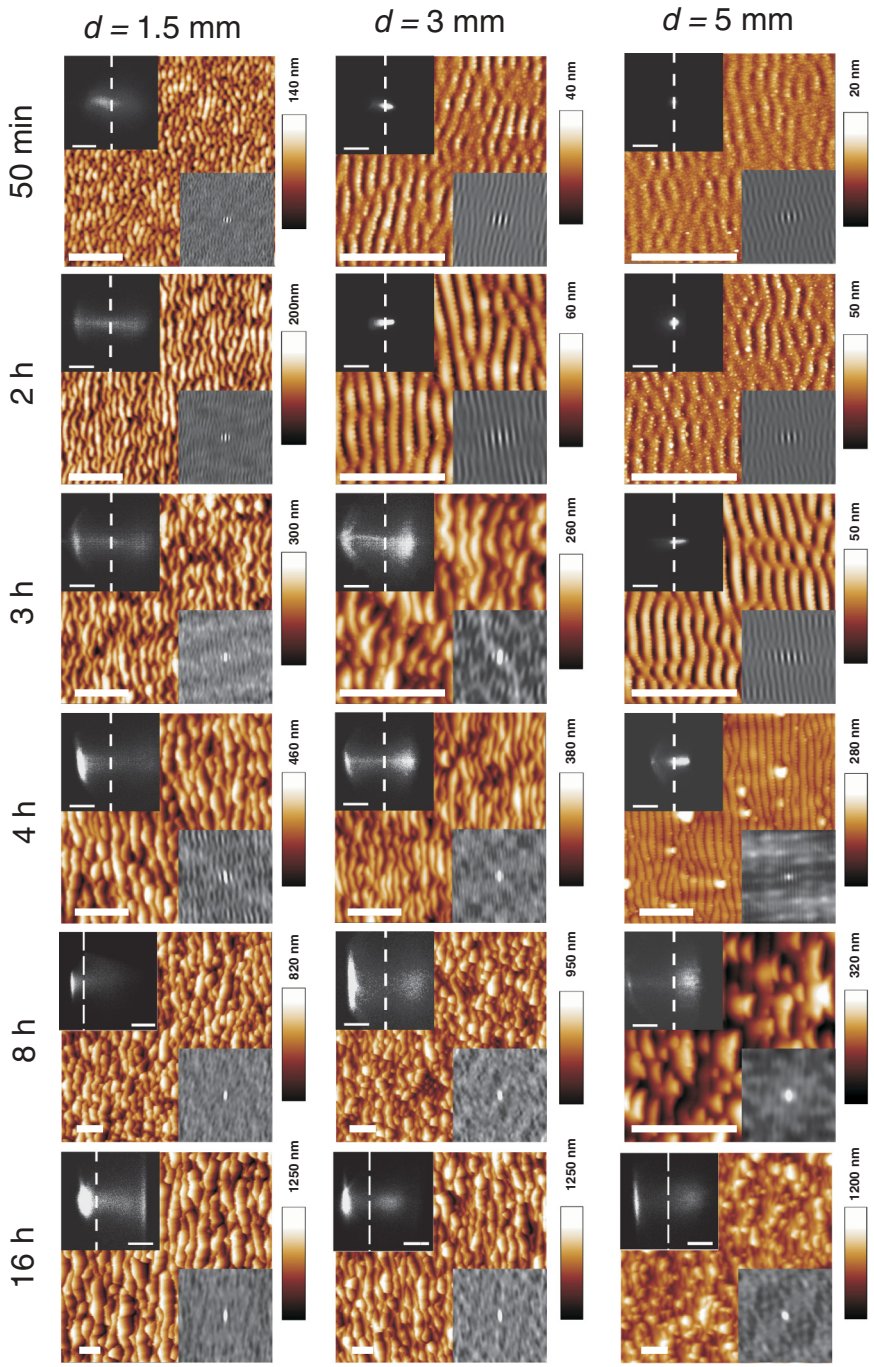

FIG. 2. (Color online) AFM images of the Si irradiated surfaces measured at d = 1.5, 3, and 5 mm (left, middle, and right columns, respectively) away from the steel target. The bombarding times are 50 min, 2 h, 3 h, 4 h, 8 h, and 16 h (from top to bottom). The ion beam goes from the left to the right of the images, whereas the direction of the Fe flux is the opposite. The horizontal bars correspond to 2.5 μm. The insets show two-dimensional autocorrelation (bottom) and slope distribution (top) functions. In the latter, the x and y axis mean the derivative of the surface height along the corresponding directions, and the scale bar corresponds to 0.5 except for 1 mm/8 h, 3 mm/16 h (0.75), and 1 mm/16 h (1). The dashed vertical line indicates the null horizontal slope value in order to better show the eventual asymmetry of the slope distribution.

This feature is a further indication that Fe atoms do not form Fe metallic clusters on the surface, but are incorporated into the outermost layers of the Si matrix forming semiconducting silicides with different compositions as determined by the XPS profile shown in Fig. 1(b).[46] In addition, the lack of a significant contribution of Fe-Fe bonds to the XPS spectra and the average surface composition confirm that a large fraction of Si atoms are also found at the surface layers despite the concurrent intense incoming (low-energy) Fe flux. The presence of Si at the surface can be explained by different processes, such as atom displacements or/and flow towards the surface due to spike effects associated with the high-energy ion impacts as found in metal systems,[47,48] ion-induced intermixing,[41] and higher ion-induced mobility of lighter elements (Si).[49] Note that these effects would be enhanced at the ion energy range employed in our system.[41]

B. Morphological analysis of the ion-induced patterns

In Fig. 2 the characteristic surface morphologies at d = 1.5, 3, and 5 mm are displayed for different irradiation times. Clearly rippled or facetted patterns evolve with the wave vector parallel to the ion beam projection on the surface (the Ar^+ beam coming from left to right and the Fe flux in the opposite direction, in all cases). Each image has two insets: the bottom one is the corresponding two-dimensional (2D) autocorrelation, whereas the top one is the 2D slope distribution. This latter inset is a plain two-dimensional distribution of derivatives where the horizontal and vertical coordinates on the resulting data field are the horizontal (m_x) and vertical (m_y) derivative, respectively.[38] This sort of representation is similar to that used previously for the analysis of the facet morphology of epitaxial $Si_{1-x}Ge_x$ films.[50] In our geometry, negative (positive) m_x values correspond to slopes facing the steel target (incoming ion beam). Therefore, any asymmetry along the x axis in this graph would reveal the appearance of an asymmetry in the pattern morphology with respect to the ion beam projection or pattern wave vector. Henceforth, the ripple side/facet facing the Ar^+ (Fe) flux will be denoted as front (rear) one. The corresponding roughness evolution and coarsening of the characteristic pattern wavelength λ are displayed in Figs. 3(a) and 3(b), respectively.

The AFM images themselves, together with the roughness dynamics, show that the pattern dynamics take place at a slower pace as the distance d to the metal source increases. Thus, the different pattern dynamics regimes, and the corresponding crossover times, are longer for increasing d values. However, the overall behavior of the pattern dynamics is essentially similar. This fact suggests a correspondence between erosion time and distance, that is, the pattern evolution at shorter times and distances would be equivalent to that at longer times and larger d values. Due to this equivalency, a general scenario for the pattern formation and dynamics is described below.

Initially, there is a regime in which the surface roughens due to the ion irradiation but without any hint of pattern formation (not shown). Then, a slight rippling of the surface appears, which is better observed for large d values. An interesting feature of this emerging ripple structure is that the rear (negative) ripple slopes are steeper than the front (positive)

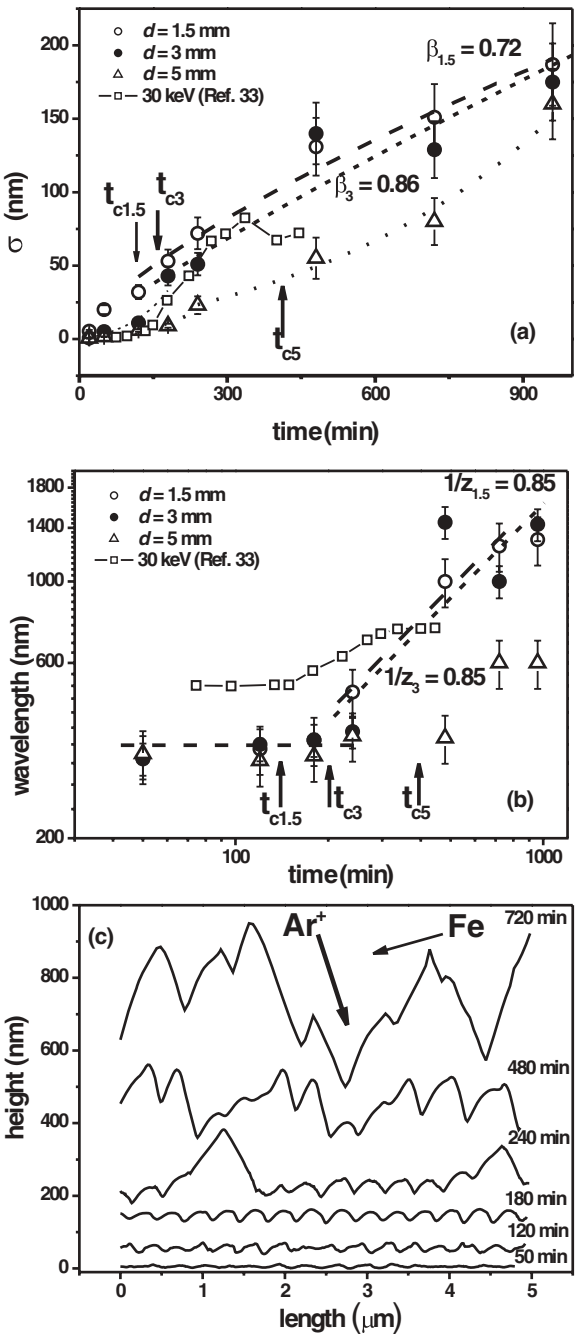

FIG. 3. Plot of (a) the surface roughness and (b) the pattern wavelength as a function of the irradiation time for the three locations on the Si target surface, d = 1.5, 3, and 5 mm, away from the metal source. For each data set, the roughness dependence on time (dashed, short dashed, and dotted lines, respectively) as well as the coarsening observed for late times for the 1.5 and 3 mm cases are indicated. The horizontal dashed line in (b) indicates the initial regime without coarsening. Also, the respective estimated crossover times (t_c) for which shadowing (see discussion) starts to operate are indicated with arrows. In both figures, the corresponding values obtained in Ref. 33 are plotted [in (a), the roughness amplitude instead of σ is plotted]. (c) Typical surface profiles for different irradiation times for the Si location at 5 mm from the metal target. The surface profiles have been shifted upwards with increasing time for clarity. The ion beam and Fe flux directions are indicated.

ones since the lateral distance between the high-ripple ridge (brightest spot) and the closest deep valley minimum (darkest spot) is shorter at the right side of the ridge than at its left side. As the 2D autocorrelation shows (bottom inset of Fig. 2), the pattern already has a short-range ordering. In addition, nanostructures scattered over the surface can be detected. A detailed inspection of these structures reveals that those located on top of the ripples along the ripple direction are higher (4–5 nm high) and wider. Accordingly, we refer to them as dotlike features. Furthermore, as the irradiation proceeds, this ripple morphology becomes more homogeneous, displaying a clear ordering (see corresponding bottom insets in Fig. 2) and an array of dot structures with lateral sizes of 80–100 nm and heights of 3–8 nm which self-organize along the rear ripple edges (those facing the Fe flux direction). The ripple pattern order enhancement can be quantified by analyzing the ratio between the $PSD_{\parallel}$ peak at full width at half maximum (FWHM) and the peak position (i.e., $k_0 = 1/\lambda$).[51] This analysis has been performed at $d = 5$ mm, because of the slower dynamics, and confirms the pattern order enhancement during this dynamic regime.[40] In addition, at this stage, the ripple morphology becomes clearly asymmetric, which is revealed in the corresponding asymmetric intensity distribution of the surface slope as the contribution from positive m_x values is more intense (Fig. 2, $d = 3$ mm at 2 h and $d = 5$ mm at 3 h). This feature of the slope distribution function is due to the fact that more surface sites lie on low sloped regions (those at the left side of the ripple maxima, facing the ion beam). Within this regime, σ increases exponentially [Fig. 3(a)], while λ is constant [Fig. 3(b)].

Eventually, this ripple pattern decorated by the dot array evolves into a rougher facetted pattern, with a crossover time which is longer for larger d values. This transition can be glimpsed for $d = 5$ mm (Fig. 2, at 4 h) due to its slower pattern dynamics. Here, the decorated ripple pattern morphology is still observed as well as larger three-dimensional (3D) structures (around 130 nm high) scattered on the surface and preferentially placed on the ripple edge facing the metal source [see Figs. 2 and 3(c)]. After 8 h, a close inspection of the corresponding AFM image reveals that, although few dots decorating the ripple structures survive, for the most part the surface is formed by asymmetric highly facetted structures with the larger slopes facing the metal target [Fig. 3(c)].

The last regime of the pattern dynamics consists of the further evolution of this facetted morphology, which is characterized by a marked asymmetry with respect to the ion beam direction and a poor ordering. In fact, for the longest irradiation times, the surface profile along the ion beam direction is saw-tooth-like, with the steeper side facing the incoming ion beam [Fig. 3(c)]. The lowest slope side is usually longer and displays a surface angle $\theta_x \sim -30^\circ$ (i.e., the complementary angle of the incidence angle), which corresponds to the intense and neat maximum in the slope distribution around $m_x \sim -0.6$. This final regime is characterized by steep roughness dynamics [Fig. 3(a)], with $\sigma \propto t^{0.75}$ ($d = 1.5$ mm) and $\sigma \propto t^{0.86}$ ($d = 3$ mm) together with a steep coarsening, clearly evident in the AFM images as $\lambda \propto t^{0.85}$. It seems that λ tends to saturate for the longest erosion times. It should be noted that at $d = 5$ mm the late roughness dynamics are different since they do not follow a power law behavior, but rather have a steeper exponential dependence together with a higher λ value. In this sense, it is necessary to note that for this farthest location, the surface morphology homogeneity is not as evident as in the other two cases. This could be due to the lesser and more inhomogeneous incoming Fe flux reaching this large d value. Therefore, larger error bars should be considered for the roughness and wavelength values in Figs. 3(a) and 3(b).

C. Lateral and *in-depth* distribution of Fe in the facetted pattern: Compositional patterning

In order to obtain further information about the metal location on the irradiated targets, we have studied by TEM (Fig. 4) the structure and composition of the facetted pattern formed after 16 h of irradiation at a distance d in the 1–2 mm range. Figure 4(a) shows a bright-field TEM image where the contrast is given by the electron absorption and, hence, darker regions represent denser or thicker areas, as well as oriented crystals with respect to the electron beam. A clear saw-tooth-like surface morphology, with the lowest slope facing the steel target, is observed in agreement with AFM observations. The a-layer induced by the Ar^+ beam impingement on the surface (brighter region) is clearly observed, with a thickness of ~110 nm at those facets facing the direct ion beam. This value was compared with that obtained from Monte Carlo simulations of TRIM code assuming that the a-layer expands up to the maximum of the ion range distribution, which is defined as the mean projected ion range plus three times the longitudinal

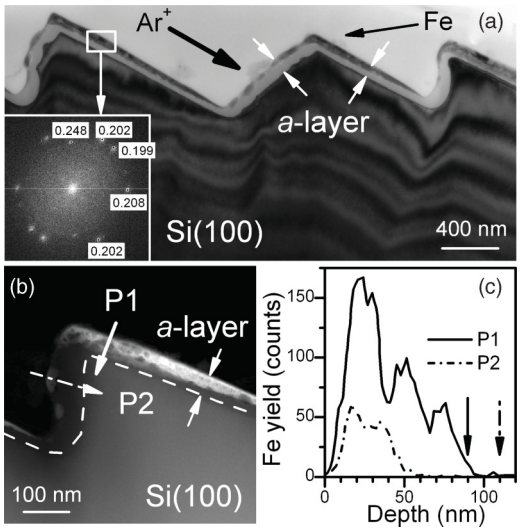

FIG. 4. (a) Bright-field TEM image of the ripple structure formed at 1–2 mm from the Fe source after 16 h of irradiation. Note the continuous Fe-rich slab on the rear ripple sides in contrast to the discontinuous Fe agglomeration on the front sides. The Ar^+ beam and Fe flux directions are indicated. The inset shows FFT corresponding to the region defined by the white square showing the formation of nanocrystals. (b) HAADF image of a ripple showing in bright contrast the zones with heavier elements. The dashed line highlights the interface between the a-layer and the crystalline Si beneath. (c) EDX Fe profiles taken from line scans along the front (dashed line) and rear (solid line) sides of the ripple at the locations marked by the arrows in (b). The vertical arrows in (c) indicate the a-layer thickness for both locations.

straggling.[52] Under these conditions, where the ions impinge almost under normal incidence on the front facet, a value of 104 nm is obtained, in agreement with the measured one. For the rear facet, the a-layer is ∼90 nm at those locations close to the ridge, whereas it is ∼75 nm close to the bottom apex. In this facet, the beam impinges almost parallel to the surface and the thickness of the amorphous layer can be estimated by the radial range of the ions plus three times the radial straggling.[52] This estimation leads to a value of 54 nm, which is close to the experimental value (note that the value may be larger taking into account the beam divergence).

In the outer part of the a-layer, a darker slab is observed corresponding to denser material. Therefore, they can be correlated with Fe-rich domains. According to our XPS results, these domains should be ascribed to silicide regions. Furthermore, the lack of structure in the TEM image is an indication that the silicides are mostly amorphous as has been reported for ion-beam mixing of Fe/Si bilayers.[53] The silicide slab is more homogeneous over the rear facet although it displays a decreasing thickness from peak (∼65 nm) to valley (∼0 nm), likely due to the shadowing effect imposed on the incoming Fe flux by the saw-tooth-like morphology. In contrast, this Fe-rich slab is rather discontinuous or absent on the front facets, for which the ion beam impinges practically under normal incidence. Here, Fe-rich silicide regions can vary from relatively large values, such as ∼50 nm, to practically zero.

A closer inspection of the front slab morphology, as well as of that of the underlying crystalline regions, reveals that the presence of these Fe-rich domains on the front sides induces the existence of a rather correlated corrugation on the underneath interface between the a-layer and the crystalline Si. This correlated corrugation can be appreciated particularly in the left and middle facets facing the ion beam in Fig. 4(a). This fact is likely due to a masking effect by the denser Fe-rich (silicide) domains that reduce the ion penetration range with respect to pure Si regions. Under this scenario, the underlying Si bulk corrugation would merely reflect the Fe distribution over the top facet under normal ion incidence. It is interesting to note that this effect is not so evident on the rear sides facing the metal source, probably due to the almost grazing incidence of the Ar^+ ions on these facets. Another noticeable feature revealed by the TEM analysis is the concave morphology observed at the bottom of the front sides, clearly seen in the two extreme structures of Fig. 4(a), which is found at the surface of both the amorphous layer and the interface with the crystalline Si phase. This fact is an indication of ion sputtering enhancement at this location. The reason for such enhancement is likely to be the reflection of Ar^+ ions impinging near the bottom of the adjacent rear facet. Likewise, part of the Fe-rich structures observed on the front sides could correspond to Fe re-sputtered from the contiguous frontal rear one.

The analysis of the Fe-rich domains in the rear facets reveals some differences with respect to those found on the front ones. Thus, it is found that Fe aggregates are indeed located at, but not strictly restricted to, the outmost surface. Interestingly, some of them are found to be buried to some extent. Imaging the darkest regions inside the a-layer with atomic resolution reveals the sporadic formation of nanocrystalline grains within the amorphous silicide matrix. As an example, the fast Fourier transform (FFT) corresponding to the enclosed region within the white square in the image is depicted in the inset of Fig. 4(a). We identified the main experimental FFT spots as those of the β-$FeSi_2$ phase (see a detailed discussion in Ref. 40). The β-$FeSi_2$ phase is one of the few stable phases of iron silicide at room temperature,[54] although the formation of crystalline β-$FeSi_2$ by ion beam mixing (equivalent to our experimental conditions) normally requires relatively high temperatures (∼500 °C).[55] This fact suggests that the formation of β-$FeSi_2$ might require not only the appropriate metal to silicon ratio at the surface, but also a significant increase of the local temperature during the implantation. This temperature rise during energetic collision cascades is a well-known phenomenon explained by the thermal spike model.[56] Experimental evidence of this fact has already been reported for Si/Fe bilayers implanted with noble gas at room temperature, and explained on the basis of chemically guided atomic diffusion in the presence of local thermal spikes.[49] Moreover, it has been proposed that the amorphized state of the silicon matrix enhances the ion beam mixing,[53] a scenario that certainly applies to our system and that would be more relevant than in low-energy IBS where appreciably thinner a-layers are formed.[10]

Figure 4(b) shows a high angle annular dark field (HAADF) image of one of the saw-tooth-like structures. Here, the image provides direct Z contrast enabling the identification of different elements. Clearly the correlation between the darker zones in the bright-field image and the presence of Fe is further supported. Moreover, we can see that the Fe content in the rear facet and close to the peak can extend even up to the interface between the a-layer and the unaltered crystalline Si beneath. The Fe profiles obtained by EDX in both facets (line scans along the directions marked by the arrows) are depicted in Fig. 4(c). The profile along the rear facet (P1) shows that Fe is indeed distributed over an 80 nm depth range, corresponding to the whole a-layer thickness, with a maximum Fe content closer to the surface (at ∼35 nm). The peaks resolved along the profile are due to the presence of Fe-rich nanostructures similar to those discerned in the main white slab of Fig. 4(b). These results indicate that Fe has an inhomogeneous in-depth distribution giving rise to (Si-rich) silicide regions with decreasing Fe content at larger depths. In contrast, the profile recorded through the front face (P2), where the a-layer is thicker (∼110 nm), reveals a narrower and shallower Fe distribution confined to within the first 40 nm. In addition, the Fe content is a factor of 3 lower than the one observed in the rear facet. In summary, TEM, RBS, and XPS results evidence that Fe is incorporated on the Si surface forming silicides mostly in an amorphous state and with a variable composition (Fe/Si ratio) that depends on both the surface morphology and depth.

We have further confirmed the different metal content of both facets at a larger scale using two additional techniques.[40] On the one hand, we have performed SEM analysis and obtained the relative Fe content on both sides by EDX.[40] The Fe content was found to be four times larger at the rear sides than at the front ones, which is in relatively good agreement with TEM observations. On the other hand, confirmation of the different Fe content of both facets has also been obtained from XPS spectra acquired at different take-off angles of the sample surface with respect to the detector.[40]

In order to further confirm the different Fe content of both facets in the nanoscale range, we have characterized some samples by C-AFM based on the premise that higher current will be extracted from silicide (nano)structures with higher Fe content. In Figs. 5(a) and 5(b) we show the AFM and C-AFM images, respectively, of the same area of the sample irradiated for 8 h at $d = 1.5$ mm when a clear facetted pattern has developed. There is an evident correlation between the facetted morphology and the current mapping. More specifically, the highest current spots take place mainly at the rear facets and near the highest ridge. These surface locations correspond to those locations with a higher Fe concentration as assessed by TEM. Therefore, TEM, SEM, XPS, and C-AFM data confirm that the asymptotical facetted pattern displays a preferential silicide formation at the rear facets.

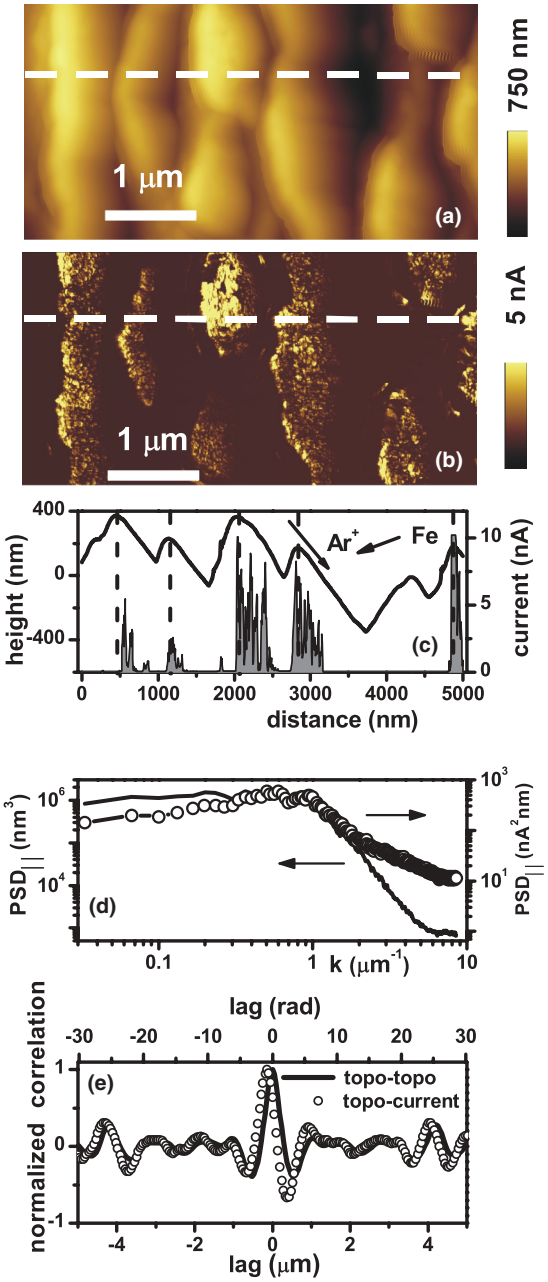

FIG. 5. (Color online) (a) Topographical and (b) C-AFM images measured simultaneously on well developed facetted structures located at $d = 1.5$ mm after 8 h. (c) Corresponding topographical (solid line) and current (gray-filled curve) cross-section profiles along the dashed line in (a) and (b). The vertical dashed lines mark the top ridge locations. (d) $PSD_{\parallel}$ obtained on simultaneous AFM and C-AFM images taken on a large area. (e) Correlation between current and topographical patterns (open symbols) along the pattern wave vector direction. The autocorrelation of the topographical data (solid line) is also shown as a guide.

IV. DISCUSSION

A. Pattern dynamics by medium-energy IBS: Comparison with metal-free conditions

In this section we address the characterization of the observed pattern dynamics and its comparison with that reported previously for medium-energy Ar^+ ion bombardment of Si surfaces under a similar oblique incidence but without simultaneous metal incorporation.[33,34]

One important geometrical mechanism that can operate during the ripple pattern development induced by oblique ion bombardment is the so-called *shadowing* process. It takes place when the local slopes of a sinusoidal ripple structure become so high that part of the upstream face of the sinusoid is shadowed from the incident ion beam by the preceding peak.[57] Under these conditions, the sinusoidal wave pattern would evolve towards a saw-tooth pattern morphology as indeed occurs in our case for long irradiation times [see Figs. 2 and 3(c)]. The threshold for the operation of these shadowing mechanisms for a given incident angle α, a sinusoidal morphology with roughness σ (proportional to the ripple amplitude), and wavelength λ can be estimated from the geometrical relation given by $\tan(\pi/2-\alpha) \geqslant 2^{3/2}\pi\sigma/\lambda$.[57] Thus, for our system, shadowing will operate for $\sigma/\lambda \leqslant 0.065$. Accordingly, we have marked in Figs. 3(a) and 3(b) the approximate location of this threshold for the three d values studied. However, it is worth noting that this is a rough estimate since neither is the surface morphology homogeneously rippled (Fig. 2), nor is the ripple pattern perfectly sinusoidal for erosion times shorter than the corresponding thresholds. Moreover, it should be noted that for the $d = 5$ mm location, this threshold becomes even more ambiguous given the observed surface morphology heterogeneity. In any case, it is indeed true that for longer irradiation times the surface morphology is saw-tooth-like and displays a clear facetted pattern as expected for asymptotic behavior under shadowing processes. It is observed that around the threshold time for $d = 1.5$ and 3 mm [Figs. 3(a) and 3(b)], there is also a crossover in the surface roughening behavior that corresponds to the transition from the ripple pattern to the facetted one. Furthermore, from this threshold time, the roughening dynamics changes from an exponential to a power-law dependence as $\sigma \propto t^{0.72}$ and $\sigma \propto t^{0.85}$, respectively. Likewise, in both cases, this threshold also marks the crossover from an initial absence of coarsening of the ripple pattern for short irradiation times to an evident coarsening for the facetted pattern as $\lambda \propto t^{0.85}$. The roughening and coarsening exponents of this second regime, which corresponds to the facetted morphology, imply a rather similar growth in both the horizontal and the vertical directions. This kind of sympathetic

increase of the facetted structure amplitude and wavelength has been previously found in other studies of Si irradiated with inert gas ions.[58–61] Moreover, in these systems it was found that the facet inclinations present a bimodal behavior being close to the parallel or normal directions with respect to the ion flux trajectory, a condition that is also fulfilled in our system [see the asymptotical bimodal slope distributions in Figs. 2, 3(c), and 4(a)]. Finally, from the evident correlation between the appearance of shadowing and coarsening processes, the threshold times marked in Figs. 3(a) and 3(b) can be taken roughly as a measure of the characteristic time t_c[62] separating the linear (characterized by a roughness exponential increase and absence of coarsening) and nonlinear regimes governing the height evolution of the sputtered surface.

Figures 3(a) and 3(b) show the dynamics, in terms of roughness and pattern wavelength, of the three Si target locations studied in this work together with that obtained by Chini *et al.*[33,34] on Si surfaces irradiated with 30 keV Ar^+ ions under similar conditions but without metal codeposition. Although a certain increase with ion energy of the crossover times should be expected,[14] the observed asymptotical pattern dynamics for the three metal codeposited systems is quantitatively different from the metal-free one. For the metal-free case, both λ and σ saturate within the temporal window sampled, which is half of that used in our analysis, while in our system the roughness does not saturate (although λ seems to approach a certain saturation regime). In this regime, the ripple morphology has evolved into a saw-tooth-like facetted pattern in both cases, but under metal-free conditions the roughness saturation regime was reached for ion doses in the 2×10^{18} cm^{-2} range,[33] which would correspond to ∼3.6 h of irradiation in our system (i.e., within our window of observation). This saturation behavior contrasts with the high-roughening exponents found in our case, close to 0.8, or even the exponential roughening observed at $d = 5$ mm. This is a clear indication that Fe incorporation promotes the morphological instability.[26]

On the other hand, both systems, with and without Fe codeposition, do show the existence of an initial exponential increase of σ[34] together with an initial absence of ripple coarsening. In the metal-free case, this regime is followed by a clear coarsening with exponents in the 0.5–0.7 range to finally saturate. This behavior, prior to saturation, is qualitatively and, to some extent, quantitatively similar to that observed in our system, where Fe is being incorporated into the irradiated Si surface. However, it is worth noting that despite this apparent agreement, pattern morphologies like those of Fig. 2 for $d = 3$ mm (2 h) and 5 mm (3 h), that is, ripple structures decorated by dot arrays, are never found for the metal-free conditions.

Another marked difference between the metal-free experiments and ours concerns the t_c values for the appearance of pattern coarsening since we obtain values of ∼2 h (1.5 mm), ∼3 h (3 mm), and 4-5 h (5 mm). This behavior implies that the metal incorporation also affects the initial patterning stages. This is already evident from the different initial exponential increase of the surface roughness for the $d = 3$ mm and 5 mm cases that leads to a longer t_c value for the farthest location. This fact could be also related to the different initial λ value of the ripple morphology under metal-free and metal-containing IBS [see Fig. 3(b)]. For the metal-free case,[34] this value is constant within the initial linear regime and close to 0.6 μm, a range that we have confirmed experimentally by irradiations without the steel clamp (not shown). In contrast, λ is in the 0.3–0.4 μm range when Fe is incorporated during the irradiation, regardless of the distance d with respect to the steel target. In this sense, the presence of Fe atoms on the irradiated surface affects the initial IBS rippling of the surface leading to a smaller initial λ than that observed on a clean Si surface.

B. Phenomenology of pattern formation and development for IBS with metal codeposition

From the previous analysis, as well as from the AFM images depicted in Fig. 2, it is evident that the metal codeposition during medium-energy IBS of silicon under oblique incidence does affect the pattern morphology and dynamics. In a recent paper focused on low-energy IBS under $\alpha < 45^\circ$ (where no patterning is produced on a clean surface), Macko *et al.*[30] established that the ratio between the Fe (Φ_{Fe}) and the ion (Φ_{Ar}) fluxes is a key parameter of pattern selection. Our results do confirm this statement, but also clearly show that Φ_{Fe}/Φ_{Ar} also determines the pattern dynamics (note that Φ_{Ar} is constant in this experiment). In this sense, it is interesting to note that similar pattern morphologies can be found (see Fig. 2) for different target locations, that is, different Φ_{Fe}/Φ_{Ar} values, at different doses or times (for instance, compare the morphologies at $d = 3$ and 5 mm for 2 and 3 h, respectively) despite that the Fe coverage is eight times larger at the shorter location (Fig. 1). Therefore, it is clear that Φ_{Fe} alone does not determine the pattern morphology. However, it should be noted that, in contrast to Refs. 29 and 30 the Fe contents for large d values under medium-energy irradiation have not reached yet the saturation (steady-state) levels. In fact, at $d = 3$ mm the Fe content saturation is reached for $t > 3$ h, where the facetted ripple morphology holds.

In the following, we propose a possible pathway for the observed pattern formation and dynamics. This proposal is based on previous models for the low-energy IBS systems[29,30] together with the particularities of our system configuration in terms of ion energy, angle of incidence, and geometrical setup.

1. Early stages of pattern formation

Some recent works have debated whether initial phase segregation is necessary to trigger the ripple formation or not,[29,30] especially taking into account the different sputtering yields and erosion rates at low-energy IBS. This subject becomes quite relevant since ion-induced phase separation would eventually create a compositionally modulated surface that might result in height fluctuations driven by the ensuing local composition-dependent sputter rate. In order to address this issue in our system, we have estimated the values of the sputtering yield and erosion rate for Si, Fe, and $FeSi_2$ using the TRIM code. For the $FeSi_2$ case, the cohesive energy calculated by Moroni *et al.*[63] has been used to estimate the surface binding energy, and the mass density of the compound has been taken from tabulated data.[64] We find that, under our working conditions, the sputtering rate is ∼20% lower for the $FeSi_2$ compound than for pure Si (similar to the reduction found by Macko *et al.*[30] with their setup). This

result confirms that a silicide region would be eroded at a slower rate than the surrounding silicon regions, which eventually leads to the formation of a silicide-rich surface protrusion. This scenario had already been assumed for the case of nanodot pattern formation at normal incidence with concurrent Mo deposition.[8,9] Thus, the elucidation of the role played by silicide segregation in IBS patterning of Si with Fe incorporation becomes important to determine the mechanisms that govern it.

It should be noted that in Refs. 28– 30 IBS was performed under angles below the critical value (∼45°) for pattern formation and, therefore, no patterning would be induced without the Fe supply. In our case ($\alpha = 60°$), we are above this threshold and pattern formation would be observed even in the absence of Fe, as nicely shown by the reference works of Chini *et al.*[33,34] In order to address this issue we have applied C-AFM measurements to assess at the nanoscale the possible segregation of silicide phases at this level in the initial stages of ripple formation. This analysis is made on the basis of the results of Sec. III C, where Fe-rich silicide domains yield higher intensity by C-AFM imaging.

Figures 6(a) and 6(b) show the topographic and current AFM images, respectively, taken simultaneously on the sample irradiated for 50 min at the 5 mm spot. In the first image, a rather flat morphology ($\sigma \sim 0.7$ nm) is observed. Scattered on the surface, small granular nanostructures (10–35 nm wide) with heights in the 0.5–3 nm range are found. However, two shallow ripple structures (with a peak to valley height of just 2–3 nm) are emerging in the middle right part of the image. Therefore, this image corresponds to the very early stages of ripple formation. In the corresponding current image, the brightest spots, which correspond to the Fe-rich silicide nanodomains, are not particularly associated with the emerging ripple structure since they are found either in or out of it. Moreover, the brighter current spots seem to be related to the small nanostructures found in the topographic image.

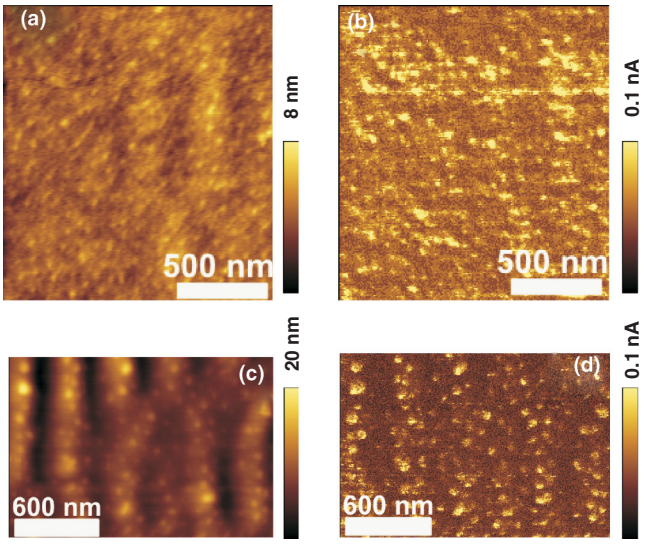

FIG. 6. (Color online) Topographical (a) and current (b) AFM images taken simultaneously on a sample irradiated for 50 min at $d = 5$ mm. Note the two incipient ripple structures emerging in the middle right part of the image (a). Topographical (c) and current (d) AFM images taken simultaneously on a sample irradiated for 50 min at $d = 4$ mm.

Further information on the pattern formation process can be obtained from Figs. 6(c) and 6(d) corresponding to a later stage of the rippling formation process. Now, clear ripples with heights in the 8–18 nm range and $\lambda \sim 330$ nm are observed. In addition, small dot structures are clearly visible with a broader height distribution (from 1 to 8 nm). The corresponding C-AFM image does show anisotropy in the spatial distribution of the high current spots as they are preferably found on top of the ripple, but not at the ripple minima, a scenario already predicted theoretically.[25]

Finally, at a later stage of this ripple formation regime (similar to that of Fig. 2 for $d = 5$ mm and 3 h), characterized by a ripple pattern together with an array of self-organized dots along the ripple edge closer to the Fe target, the dots also yield a higher C-AFM signal.[40] The dot self-organization process can be better appreciated in the $\mathrm{PSD}_\perp$ curves corresponding to the early patterning stages[40] since a small but clear peak or kink is defined. This feature indicates the presence of a characteristic dot-dot distance along the direction perpendicular to the ripple wave vector (i.e., along the ripple ridge). The $\mathrm{PSD}_\perp$ curves also show a small but noticeable coarsening with time of this dot-dot distance.[40]

The ensemble of these data allow us to conclude that on the first stages of irradiation with simultaneous Fe incorporation there is a sort of segregation of Fe-rich silicide nanodomains that are randomly scattered over the surface, without any evident correlation with the emerging ripple structures. Thus, the different erosion rates of silicide and silicon do not trigger the ripple formation for our irradiation conditions. However, the shorter initial ripple λ, compared to that obtained on clean Si surfaces, should be related to the Fe presence at the irradiated surface (see Sec. IV A). Once ripples are formed, the Fe-rich silicide nanostructures are selectively formed preferentially outside of the ripple minima. This preferential formation of the Fe-rich dots is likely to be due to the rather glancing incidence of the incoming Fe flux on the surface rippled morphology. This behavior is indeed enhanced for the further stages of the ripple/dot pattern development as most of the dots are self-organized along the ripple edges facing the Fe source. As a consequence, a compositional (silicide-rich) pattern is already produced after the early stages of the ripple pattern formation. This compositional pattern also evolves into the dot array as the irradiation with concurrent Fe deposition proceeds.

This pattern formation scenario agrees with the statement of Zhang *et al.*[29] about ripple patterning under low-energy IBS with metal surfactants: "...under such conditions a ripple pattern exists before the (metal) steady-state coverage reaches its equilibrium value. The initial ripple pattern is then generated by the ion beam and the surfactants may modify this pattern." The first sentence is indeed consistent with our data for $d = 3$ mm ($t < 3$ h) and $d = 5$ mm ($t < 8$ h). In addition, the second sentence agrees with the topographic and C-AFM data obtained at the early stages of ripple formation. However, our data also show that some sort of phase segregation already exists before ripple formation but does not trigger it.

Likewise, the further pattern development seems to agree with the pattern formation description proposed by Macko *et al.*[30] for low-energy IBS. In this work, the authors proposed

that phase separation, height fluctuations, as well as the (large) angle between the ion and Fe flux directions are necessary for pattern formation and evolution. In our case, the initial ripple formation produces basically two types of height fluctuations, that is, the two slopes of the ripple morphology along its wave vector direction. One of these slopes (negative slope) faces the Fe target, whereas the other (positive) faces the ion beam. XPS data proved that the incoming Fe and Ar^+ ion fluxes landing on the surface led to the formation of silicide aggregates, which occur preferentially on the negative slope regions close to the ripple ridge. Then, as they are eroded more slowly than the surrounding areas due to their lower sputtering rate, they rise in height. Furthermore, these regions are sculpted by the ion beam and, after some time, result in local ion incidence angles beyond the maximum erosion rate (typically, $\alpha \sim 70^\circ$). Consequently, their erosion diminishes and the observed dot structures emerge at the negative slope ripple edges. Our results at this stage confirm that: (i) silicide formation and segregation play key roles, resulting in regions with different erosion rates (as shown by the emerging dots yielding higher current in C-AFM); (ii) height fluctuations (specifically, those with the local surface normal parallel to the Fe flux direction) are necessary to trigger the self-organized dot array patterning as they only emerge at the negative slope ripple edges; and (iii) that wide angles between the Fe and Ar^+ fluxes facilitate the dot patterning process as Fe-rich silicide nanostructures are preferentially formed at the ripples slopes facing the Fe source.

Finally, another interesting aspect concerns the self-organized formation of these Fe-rich silicide dots along the negative slope ripple edges. This highly ordered one-dimensional dot arrangement that coarsens with time along the ripple structures resembles those observed by Kim *et al.*[65] by sequential nanoripple and nanodot formation by low-energy IBS on Au(001) surfaces. In that case, local redeposition and surface-confined transport mechanisms were considered as essential mechanisms for both formation and preservation of the one-dimensional order of such a nanobead pattern. Although our system has strong differences with it, these effects could also play a role in this stage of the pattern dynamics.

2. *Intermediate stage: Faceting formation*

The transition from the ripple pattern regime to the facetted one is clearly manifested for $d = 5$ mm, in particular for 4 h [see Figs. 2 and 3(c), and the corresponding 3D image of the surface at this irradiation stage].[40] The small ripple structures with self-organized dots along their negative slope edges are observed coexisting with larger structures. The latter are scarcely and randomly scattered on the surface, also being found at the ripple edges facing the Fe source. A closer inspection of them shows that they become facetted on the side facing the Fe flux direction. Angles larger than 30° with respect to the horizontal direction were found close to the base, whereas smaller angles, ranging 21°–30°, were measured close to the ridge. Thus, the side of the structure facing the Fe flux is being sculpted by the incoming ion beam, already developing some sort of faceting. The fact that the initial formation of these facetted structures is so heterogeneous could be due to the sparse distribution of sputtered Fe for the largest d values. As the irradiation proceeds, new structures are formed while those formed previously enlarge resulting in a surface morphology as displayed in Fig. 2 ($d = 5$ mm, 4 h).[40] Clearly, large facetted structures have developed along the ion beam impinging direction. However, rows of aligned dots still survive on some spots. Likewise, the dot compositional pattern also evolves into a facetted morphology in which the facets facing the steel source are richer in silicide.

3. *Asymptotical stage: Marked facetted pattern morphology*

As the irradiation proceeds, a marked facetted structure develops with an evident σ and λ increase. At this stage, the ion incidence geometry on the local surface is totally altered. Once the facetted structure is fully formed, the angle distribution becomes bimodal (see the two brighter spots in the asymptotical slope distributions in Fig. 2). This structure develops since Ar^+ impinges almost under normal incidence on those sides facing the ion beam, whereas the ion beam hits practically under grazing incidence on those termed as rear sides. This asymptotic scenario has also been reported in other systems.[58–61] Obviously, as the sputtering yield depends strongly on the incidence angle,[42] the erosion rate of both sides is different, being noticeably lower for the rear sides. Similar asymptotical facetted pattern morphology has indeed been reported for Fe-free medium-energy irradiation.[33] In fact, the authors argued that the operation of the shadowing mechanisms should lead to σ saturation. As commented above, this is not the case for our Fe-containing system where σ does not saturate within our longer temporal window.

Moreover, at this asymptotical IBS stage, the rough and marked facetted saw-tooth-like pattern morphology affects the Fe flux deposition on the patterned surface as it hinders the front faces from the incoming Fe flux, whereas the rear ones are fully exposed to it. Thus, the Fe-rich silicide domains are mostly found on the rear facets [Figs. 4(a) and 5(c)]. Furthermore, the Fe-rich slab thickness observed on the rear sides in the TEM image decreases as the bottom apex becomes closer, that is, as the Fe-flux shadowing due to the adjacent upper ridge increases. This scenario also gives rise to a compositional pattern. In order to assess whether the morphological and chemical patterns do have the same periodicity, we display in Fig. 5(d) the $PSD_{\parallel}$ of the AFM (black line) and C-AFM (open symbols) images measured simultaneously on the facetted morphology. Clearly both PSD curves present a similar behavior with $1/k_0 = \lambda \sim 1.03$ μm, which indicates that both patterns have the same periodicity. In order to assess whether a certain lateral shift between both patterns exists, in Fig. 5(c) we plot the cross sections of the topography and current high resolution images displayed in Figs. 5(a) and 5(b), respectively. This analysis has been previously used to study InAs growth on vicinal GaAs (110).[66] From the comparison of both profiles, it is observed that most of the highest current spots occur at the rear facets and close to, but not at, the highest ridge of the ripple morphology. The existence of this lag between both patterns is of interest for the development of models on this sort of system.[21,67] In order to assess statistically the existence of this spatial lag, we have calculated the correlation between both patterns along

the pattern wave vector direction and the result is shown in Fig. 5(e). A certain lag close to 50 nm (i.e., close to 0.9 rad) exists. However, it should be taken into account that the C-AFM contact tips are usually wider than the standard ones. Thus, the observed lag value could be affected to some extent by a change in the contact area between tip and sample surface as the top ridge is approached.

Finally, it is interesting to note that the steady Fe surface coverage is reached precisely when the facetted morphology has developed (Fig. 1). This correlation between morphology and metal content should then be mainly related to the attainment of a steady Fe coverage at the rear facets. Moreover, the steady Fe coverage of the rear facets and the silicide preferential formation at the rear facets, together with the bimodal ion angle incidence could affect the sputtering rate ratio between both facets compared to that of the Fe-free system.[34]

V. CONCLUSIONS

From the comparison of the pattern dynamics with and without metal codeposition, it becomes evident that the metal incorporation during the medium-energy irradiation of silicon induces important changes on the pattern morphology, composition, and dynamics. We have found that both the pattern dynamics and selection depend on d and, therefore, on the ratio Φ_{Fe}/Φ_{Ar} (the larger Φ_{Fe}/Φ_{Ar} is, the faster the pattern dynamics). Moreover, the presence of codeposited metal alters both the initial ripple wavelength and the asymptotical pattern dynamics. In addition, the initial pattern formation and dynamics are slower for decreasing Φ_{Fe}/Φ_{Ar}.

We propose the following scenario for the formation and development of a morphological and compositional nanopattern. Due to the medium-ion energy and the large thickness of the ion-induced amorphous layer, thermal spike processes promote the atom diffusivity and the ion mixing, resulting in an enhanced silicide formation. Initially, the surface roughens without any hint of pattern formation and with a random segregation of some Fe-rich silicide nanostructures on the surface. With increasing irradiation time, ripple structures start to emerge without any correlation with these segregated nanostructures. However, once ripples emerge, these Fe-rich nanostructures are preferentially arranged at, and later on self-organized along, the ripple ridge facing the Fe source. This process is the combination of the reduced sputtering rate of the silicide nanostructures, the production of surface height fluctuations through the ion induced surface rippling, and the wide angle between the Ar^+ and Fe flux directions (Fe deposition occurring mainly at grazing angles). After ripple formation, a compositional pattern correlated with the morphological one is already produced. For prolonged irradiation times these dots evolve into larger structures that are finally sculpted by the ion beam. Asymptotically, these structures result in a marked facetted pattern morphology where the ion beam now impinges at normal and grazing incidence on the front and rear sides, respectively. Moreover, the compositional pattern becomes strongly correlated with the morphological facetted one. This correlation is due to the shadowing of the incoming Fe flux imposed by the facetted pattern, as well as to the irradiation geometry, which results in a preferential silicide formation at the rear facets. Thus, for our medium-energy conditions, most of the mechanisms proposed to govern the low-energy IBS of silicon with metal codeposition seem to determine the pattern formation as well, although at our energy range, the steady-state metal coverage as well as the silicide formation is considerably larger.

ACKNOWLEDGMENTS

We would especially like to thank F. Alonso for his help with the ion implantations carried out at INASMET (San Sebastian, Spain). We also want to thank Dr. M. Castro, Dr. R. Cuerno, Dr. J. Muñoz, and Dr. J. A. Sánchez-García for fruitful discussions and suggestions. This research has been funded by the Spanish 'Ministerio de Ciencia e Innovación' through Grants FIS2009-12964-C05-04, MAT2010-18432, and CSD2008-00023 and by Comunidad Autónoma de Madrid under project S2009/PPQ-1642 (AVANSENS). The ion implantation experiments at HZDR (Dresden, Germany) have been supported by the EC through the Integrating Activity "Support of Public and Industrial Research Using Ion Beam Technology (SPIRIT)" under Contract No. 227012. Finally, A.R.C. acknowledges funding from SFRH/BPD/74095/2010 (Portugal).

*Corresponding author: lvb@icmm.csic.es

[1] W. L. Chan and E. Chason, J. Appl. Phys. **101**, 121301 (2007).
[2] J. Muñoz-García, L. Vázquez, R. Cuerno, J. A. Sánchez-García, M. Castro, and R. Gago, in *Toward Functional Nanomaterials*, edited by Z. Wang (Springer, New York, 2009), pp. 323–398.
[3] C. Teichert, J. J. de Miguel, and T. Bobek, J. Phys. Condens. Matter **21**, 224025 (2009).
[4] T. W. H. Oates, A. Keller, S. Facsko, and A. Mücklich, Plasmonics **2**, 47 (2007).
[5] V. K. Smirnov, D. S. Kibalov, O. M. Orlov, and V. V. Graboshnikov, Nanotechnology **14**, 709 (2003).
[6] M. Paukshto, K. Lovetsky, A. Zhukov, V. Smirnov, D. Kibalov, and G. King, SID Symp. Dig. Tec. **37**, 848 (2006).
[7] E. J. Tocce, V. K. Smirnov, D. S. Kibalov, S. J. Liliensiek, C. J. Murphy, and P. F. Nealey, Biomaterials **31**, 4064 (2010).
[8] G. Ozaydin, A. S. Öczan, Y. Wang, K. F. Ludwig, H. Zhou, R. L. Headrick, and D. P. Siddons, Appl. Phys. Lett. **87**, 163104 (2005).
[9] C. Teichert, C. Hofer, and G. Hlawacek, Adv. Eng. Mater. **8**, 1057 (2006).
[10] J. A. Sánchez-García, L. Vázquez, R. Gago, A. Redondo-Cubero, J. M. Albella, and Z. Czigány, Nanotechnology **19**, 355306 (2008).
[11] J. A. Sánchez-García, R. Gago, R. Caillard, A. Redondo-Cubero, J. A. Martin-Gago, F. J. Palomares, M. Fernández, and L. Vázquez, J. Phys. Condens. Matter **21**, 224009 (2009).
[12] C. S. Madi, B. Davidovitch, H. B. George, S. A. Norris, M. P. Brenner, and M. J. Aziz, Phys. Rev. Lett. **101**, 246102 (2008).

[13]C. S. Madi, H. B. George, and M. J. Aziz, J. Phys. Condens. Matter **21**, 224010 (2009).
[14]M. Castro, R. Gago, L. Vázquez, J. Muñoz-García, and R. Cuerno (submitted).
[15]M. Moseler, P. Gumbsch, C. Casiraghi, A. C. Ferrari, and J. Robertson, Science **309**, 1545 (2005).
[16]M. Z. Hossain, K. Das, J. B. Freund, and H. T. Johnson, Appl. Phys. Lett. **99**, 151913 (2011).
[17]S. A. Norris, J. Samela, L. Bukonte, M. Backman, F. Djurabekova, K. Nordlund, C. S. Madi, M. P. Brenner, and M. J. Aziz, Nat. Commun. **2**, 276 (2011).
[18]R. Cuerno, M. Castro, J. Muñoz-García, R. Gago, and L. Vázquez, Nucl. Instrum. Methods Phys. Res., Sect. B **269**, 894 (2011).
[19]M. Castro and R. Cuerno, Appl. Surf. Sci. **258**, 4171 (2012).
[20]R. Gago, L. Vázquez, O. Plantevin, J. A. Sánchez-García, M. Varela, M. C. Ballesteros, J. M. Albella, and T. H. Metzger, Phys. Rev. B **73**, 155414 (2006).
[21]V. B. Shenoy, W. L. Chan, and E. Chason, Phys. Rev. Lett. **98**, 256101 (2007).
[22]R. M. Bradley and P. D. Shipman, Phys. Rev. Lett. **105**, 145501 (2010).
[23]P. D. Shipman and R. M. Bradley, Phys. Rev. B **84**, 085420 (2011).
[24]F. C. Motta, P. D. Shipman, and R. M. Bradley, J. Phys. D **45**, 122001 (2012).
[25]R. Kree, T. Yasseri, and A. K. Hartmann, Nucl. Instrum. Methods Phys. Res., Sect. B **267**, 1403 (2009).
[26]J. Zhou and M. Lu, Phys. Rev. B **82**, 125404 (2010).
[27]R. M. Bradley, Phys. Rev. B **83**, 195410 (2011).
[28]S. Macko, F. Frost, B. Ziberi, D. F. Förster, and T. Michely, Nanotechnology **21**, 085301 (2010).
[29]K. Zhang, M. Brötzmann, and H. Hofsäss, New J. Phys. **13**, 013033 (2011).
[30]S. Macko, F. Frost, M. Engler, D. Hirsch, T. Höche, J. Grenzer, and T. Michely, New J. Phys. **13**, 073017 (2011).
[31]T. K. Chini, F. Okuyama, M. Tanemura, and K. Nordlund, Phys. Rev. B **67**, 205403 (2003).
[32]D. P. Datta and T. K. Chini, Phys. Rev. B **69**, 235313 (2004).
[33]D. P. Datta and T. K. Chini, Phys. Rev. B **76**, 075323 (2007).
[34]T. K. Chini, D. P. Datta, and S. R. Bhattacharyya, J. Phys. Condens. Matter **21**, 224004 (2009).
[35]S. J. O'Shea, R. M. Atta, M. P. Murrell, and M. E. Welland, J. Vac. Sci. Technol. B **13**, 1945 (1995).
[36]A. Olbrich, B. Ebersberger, and C. Boit, Appl. Phys. Lett. **73**, 3114 (1998).
[37]C. Teichert and I. Beinik, in *Scanning Probe Microscopy in Nanoscience and Nanotechnology*, edited by B. Bhushan, Vol. 2, Chap. 23 (Springer, Berlin, 2011).
[38]D. Nečas and P. Klapetek, Cent. Eur. J. Phys. **10**, 181 (2012).
[39]J. F. Ziegler, J. P. Biersack, and U. Littmark, *The Stopping and Range of Ions in Solids* (Pergamon, New York, 1985), and also available from the website www.srim.org.
[40]See Supplemental Material at http://link.aps.org/supplemental/10.1103/PhysRevB.86.085436 for RBS, SEM, AFM C-AFM, and XPS data (the latter as a function of the emission take-off angle), as well as for the estimation of ripple pattern order enhancement with time through the PSD analysis, and the identification of the β-$FeSi_2$ phase from the FFT data shown in the inset of Fig. 4.
[41]R. S. Averback and P. Bellon, in *Materials Science with Ion Beams*, edited by H. Bernas, Chap. 1 (Springer, Berlin, 2010).
[42]R. Behrisch and W. Eckstein, *Sputtering by Particle Bombardment* (Springer, Berlin, 2007).
[43]V. Kinsinger, I. Dezsi, P. Steiner, and G. Langouche, J. Phys. Condens. Matter **2**, 4955 (1990).
[44]D. Briggs and M. P. Seah, *Practical Surface Analysis: Auger and X-ray Photoelectron Spectroscopy*, Vol. 1 (Wiley, New York, 1990).
[45]S. Doniach and M. Sunjic, J. Phys. C **3**, 285 (1970).
[46]S. Hong, P. Wetzel, G. Gewinner, D. Bolmont, and C. Pirri, J. Appl. Phys. **78**, 5404 (1995).
[47]M. Ghaly and R. S. Averback, Phys. Rev. Lett. **72**, 364 (1994).
[48]T. Michely and C. Teichert, Phys. Rev. B **50**, 11156 (1994).
[49]S. Dhar, P. Schaaf, N. Bibić, E. Hooker, M. Milosavljević, and K. P. Lieb, Appl. Phys. A **76**, 773 (2003).
[50]M. A. Lutz, R. M. Feenstra, P. M. Mooney, J. Tersoff, and J. O. Chu, Surf. Sci. **316**, L1075 (1994).
[51]T. Bobek, S. Facsko, H. Kurz, T. Dekorsy, M. Xu, and C. Teichert, Phys. Rev. B **68**, 085324 (2003).
[52]K. Nordlund, J. Keinonen, E. Rauhala, and T. Ahlgren, Phys. Rev. B **52**, 15170 (1995).
[53]N. Bibić, V. Milinović, K. P. Lieb, M. Milosavljević, and F. Schrempel, Appl. Phys. Lett. **90**, 051901 (2007).
[54]N. Dahal and V. Chikan, Chem. Mater. **22**, 2892 (2010).
[55]M. Milosavljević, S. Dhar, P. Schaaf, N. Bibić, Y.-L. Huang, M. Seibt, and K. P. Lieb, J. Appl. Phys. **90**, 4474 (2001).
[56]I. P. Jain and G. Agarwal, Surf. Sci. Rep. **66**, 77 (2011).
[57]G. Carter, J. Appl. Phys. **85**, 455 (1999).
[58]G. W. Lewis, M. J. Nobes, G. Carter, and J. L. Whitton, Nucl. Instrum. Methods **170**, 363 (1980).
[59]V. Vishnyakov, G. Carter, D. T. Goddard, and M. J. Nobes, Vacuum **46**, 637 (1995).
[60]G. Carter and V. Vishnyakov, Surf. Interface Anal. **23**, 514 (1995).
[61]G. Carter, V. Vishnyakov, Y. V. Martynenko, and M. J. Nobes, J. Appl. Phys. **78**, 3559 (1995).
[62]S. Park, B. Kahng, H. Jeong, and A.-L. Barabási, Phys. Rev. Lett. **83**, 3486 (1999).
[63]E. G. Moroni, W. Wolf, J. Hafner, and R. Podloucky, Phys. Rev. B **59**, 12860 (1999).
[64]D. R. Lide, ed., *CRC Handbook of Chemistry and Physics*, 87th ed., Sec. III (Taylor and Francis, Boca Raton, FL, 2006).
[65]J.-H. Kim, N.-B. Ha, J.-S. Kim, M. Joe, K.-R. Lee, and R. Cuerno, Nanotechnology **22**, 285301 (2011).
[66]P. Tejedor, L. Díez-Merino, I. Beinik, and C. Teichert, Appl. Phys. Lett. **95**, 123103 (2009).
[67]R. M. Bradley, Phys. Rev. B **85**, 115419 (2012).